Supporting Information

Phthalocyanine-Induced Iron Active Species in Metal-Organic Framework-Derived Porous Carbon for Efficient Alkaline Zinc-Air Batteries

Cheng Han[a], Xiaodeng Zhang[a], Qiuhong Sun[a], Dandan Chen[a], Tingting Miao[a], Kongzhao Su[b], Qipeng Li[b,c], Jinjie Qian*[a,b]] and Shaoming Huang[d]

[a]Key Laboratory of Carbon Materials of Zhejiang Province, College of Chemistry and Materials Engineering, Wenzhou University, Wenzhou, Zhejiang, P. R. China

[b]State Key Laboratory of Structural Chemistry, Fujian Institute of Research on the Structure of Matter, Chinese Academy of Sciences, Fuzhou, Fujian, P. R. China

[c]College of Chemistry and Chemical Engineering, Zhaotong University, Zhaotong, Yunnan, P. R. China

[d]School of Materials and Energy, Guangzhou Key Laboratory of Low-Dimensional Materials and Energy Storage Devices, Guangdong University of Technology, Guangzhou, P. R. China

*Corresponding author

E-mail: jinjieqian@wzu.edu.cn

Table of Content

General Instruments.

Scanning electron microscopy (SEM) data were obtained within a JSM-6700F field emission scanning electron microscope at 10 kV. High-resolution transmission electron microscope (HR-TEM) and energy dispersive spectroscopy (EDS) were collected on a JEOL JEM2100F microscope at a high voltage of 200 kV. Single gas adsorption/desorption were performed in the Accelerated Surface Area and Porosimetry System 2020 (ASAP 2020), and the N_2 sorption was at 77 K. The powder X-ray diffraction patterns (PXRD) were acquired with a Bruker D8 Advance using Cu Kα radiation (0.154 nm). Raman spectra were obtained in a Renishaw instrument (in Via-Reflex) with the 532 nm wavelength. X-ray photo electron spectroscopy (XPS) characterizations were carried out on a high resolution electron energy analyzer (Gamma data-Scienta SES 2002) using monochromatic Al Kα X-rays. The information on fraction and structure was obtained by a Rigaku Mercury CCD diffractometer applied with a graphite-monochromated Mo Kα radiation (0.71073 Å) at 293 K.

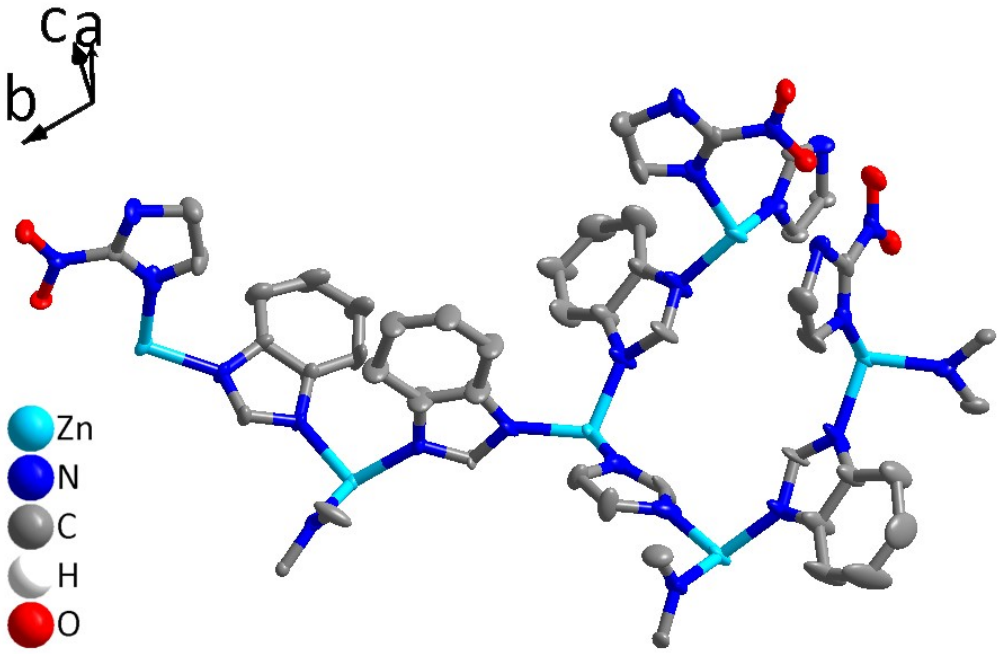

Figure S1. Asymmetric Unit (AU) of **BMM-14** without H atom.

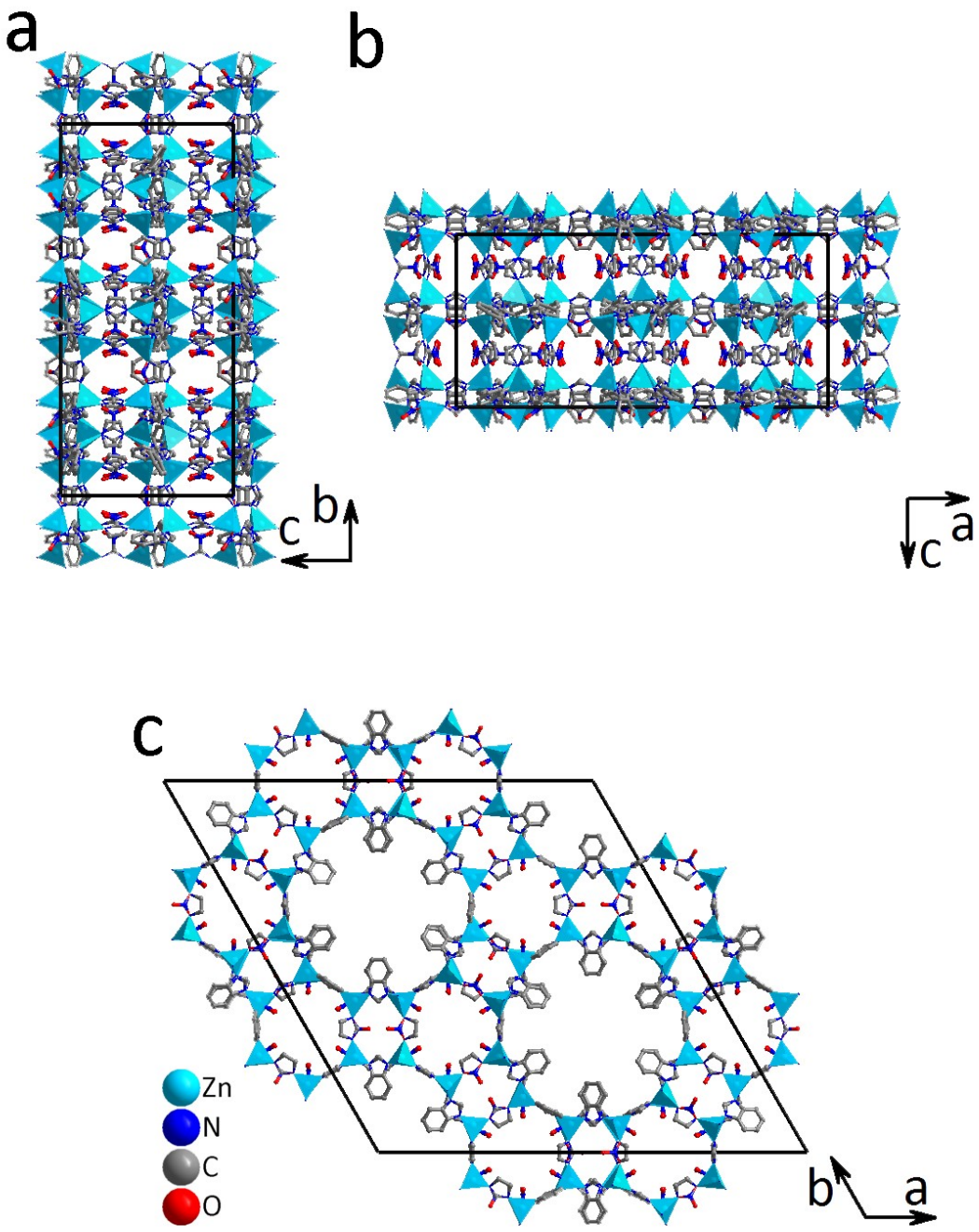

Figure S2. Structure of **BMM-14** along (a) *a* aix; (b) *b* aix and (c) *c* aix

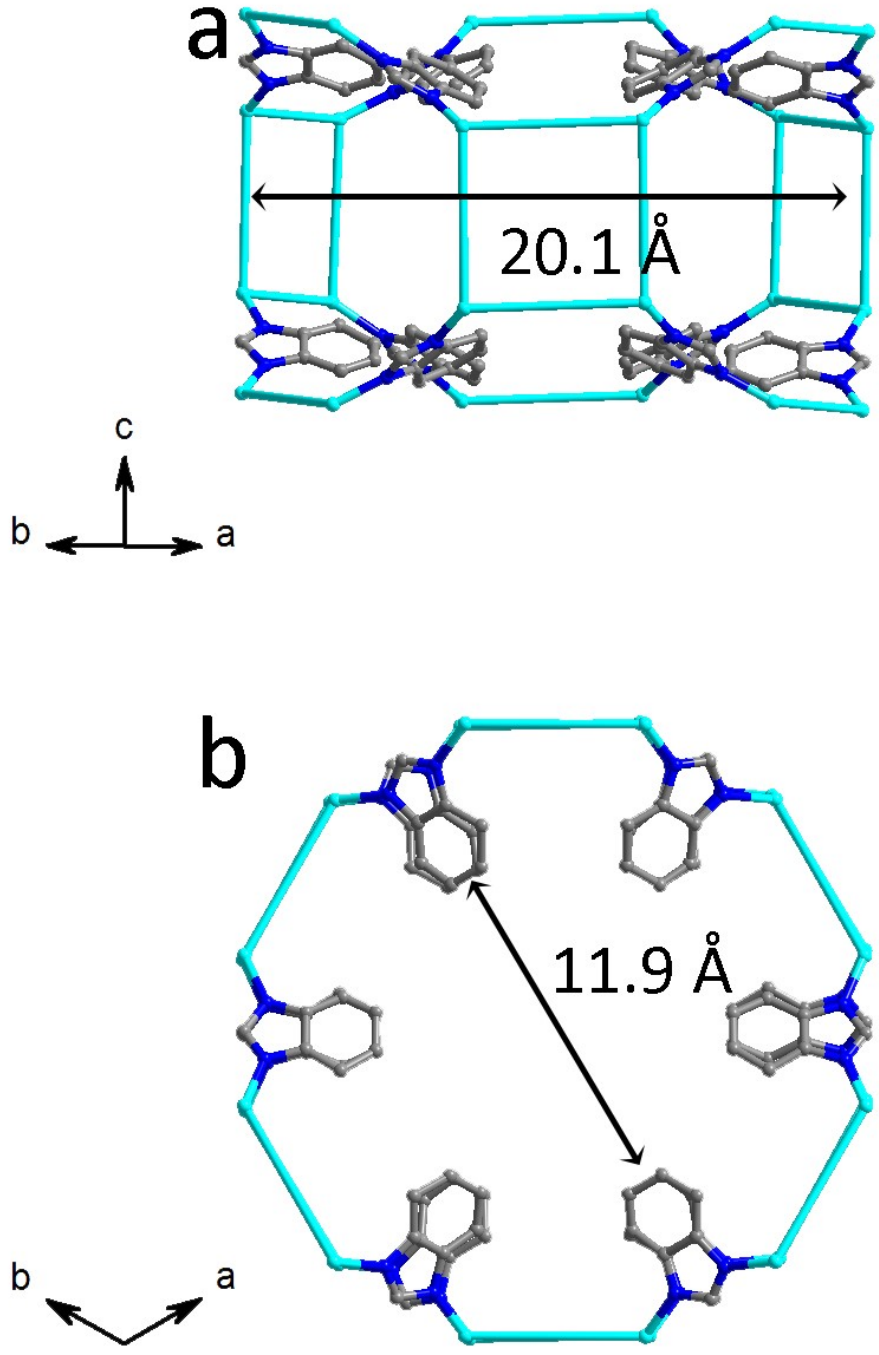

Figure S3. The influence of bIm on the channel width in the **BMM-14** structure, except for the bIm along the *ab* plane, the other ligands are replaced by stick models.

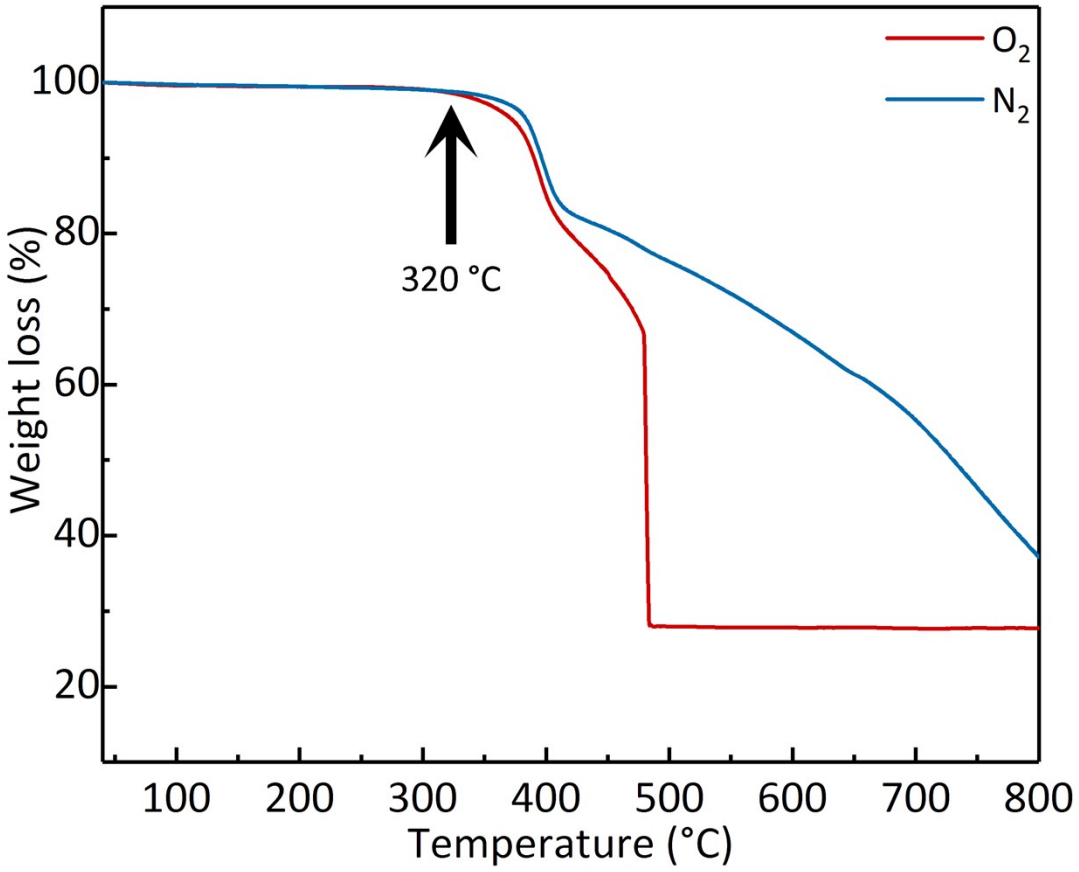

Figure S4. Thermogravimetric analysis (TGA) curves of **BMM-14** in N_2 and O_2 atmosphere.

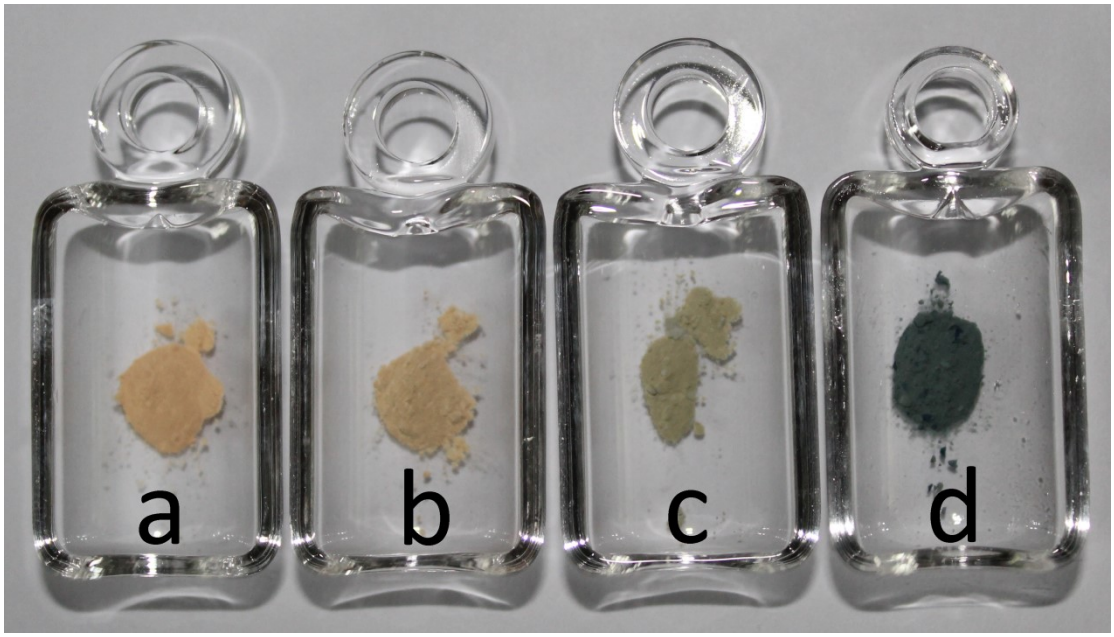

Figure S5. The color of (a) **FePc@BMM-14(0)**, (b) **FePc@BMM-14(0.1)**, (c) **FePc@BMM-14(1)** and (d) **FePc@BMM-14(10)** after dispersion.

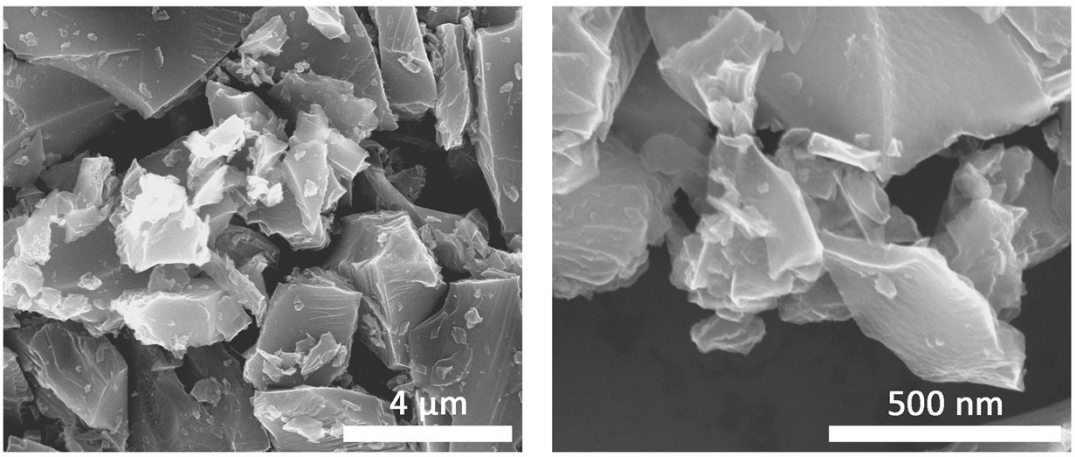

Figure S6. SEM of **FePc@BMM-1(0)**.

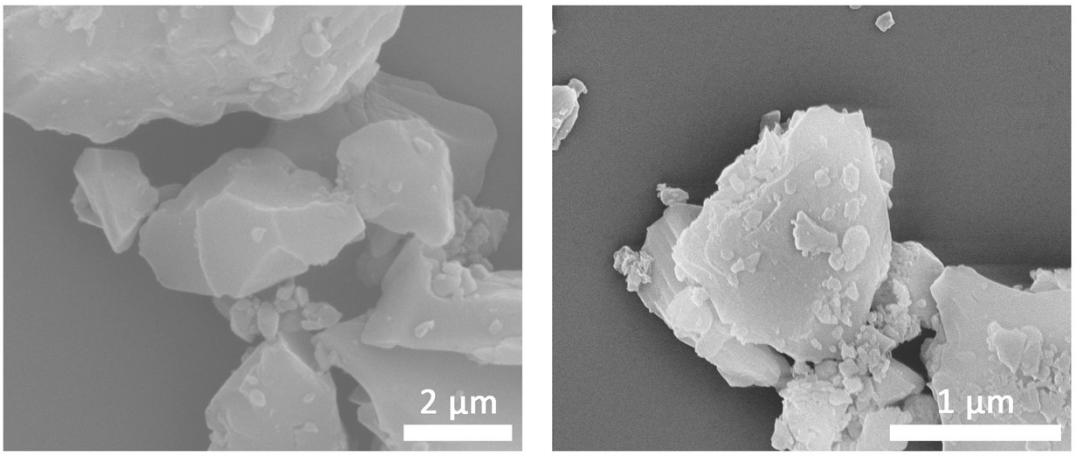

Figure S7. SEM of **FePc@BMM-1(0.1)**.

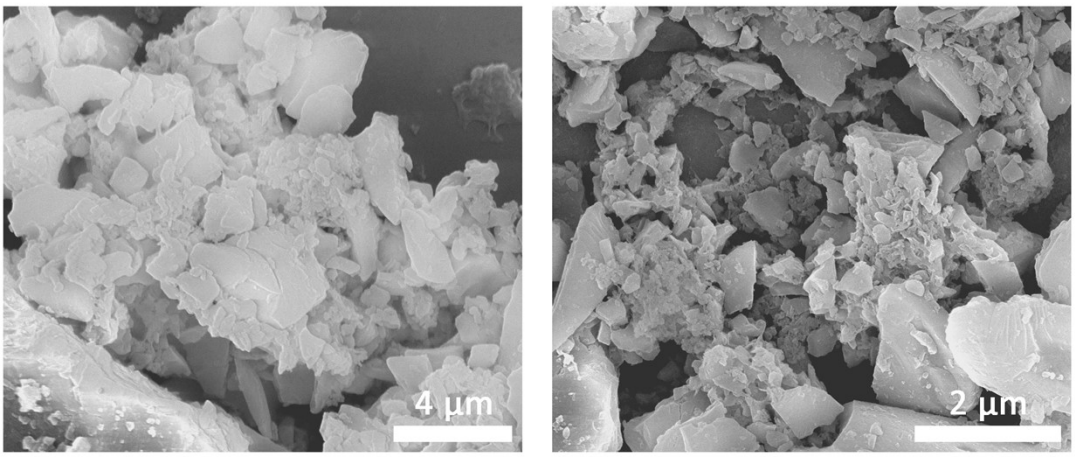

Figure S8. SEM of **FePc@BMM-1(1)**.

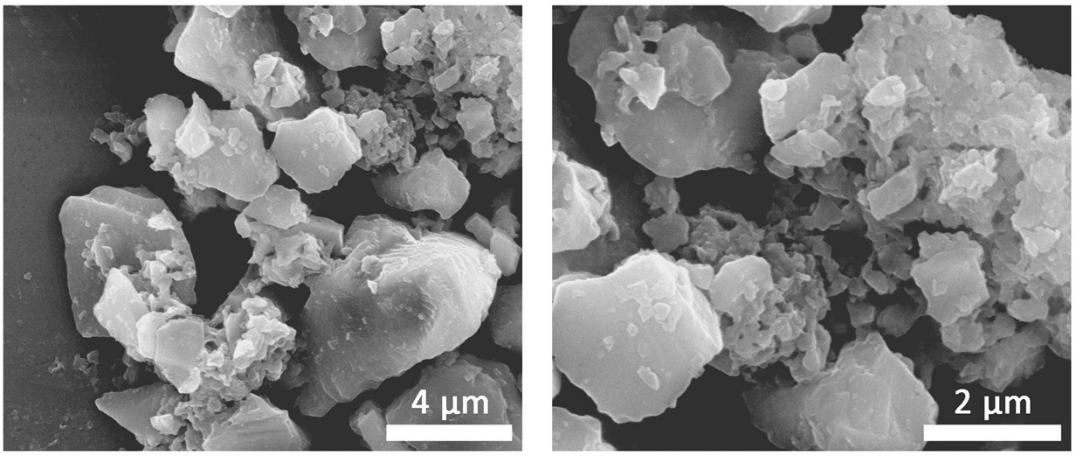

Figure S9. SEM of **FePc@BMM-1(10)**.

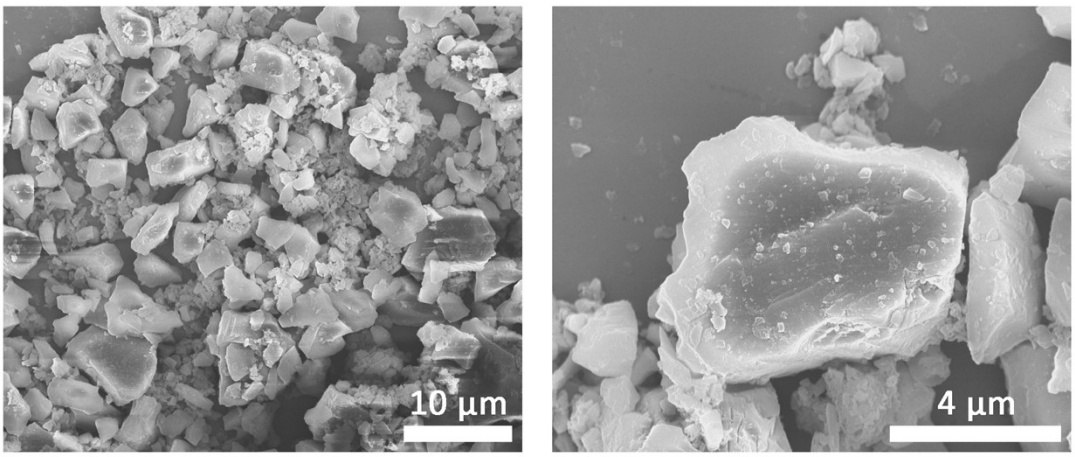

Figure S10. SEM of **Fe@NC(0+900)**.

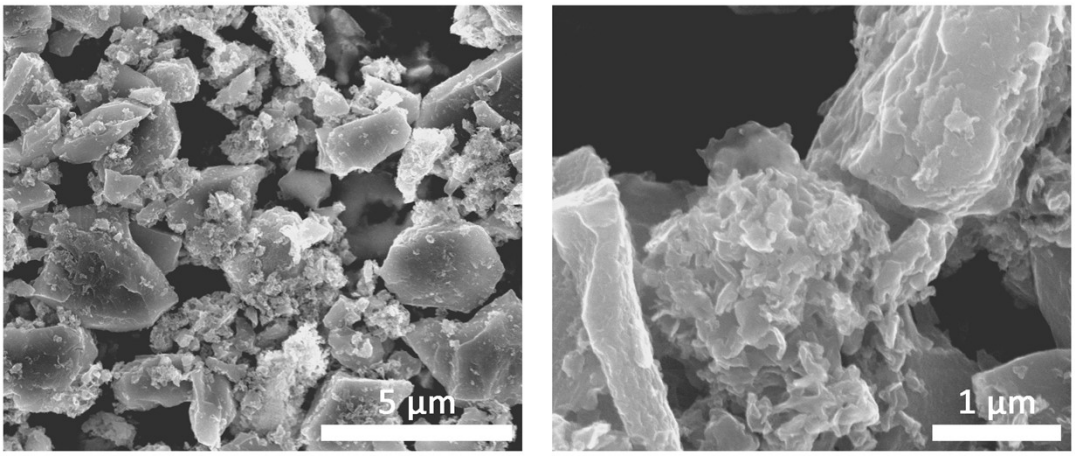

Figure S11. SEM of **Fe@NC(10+700)**.

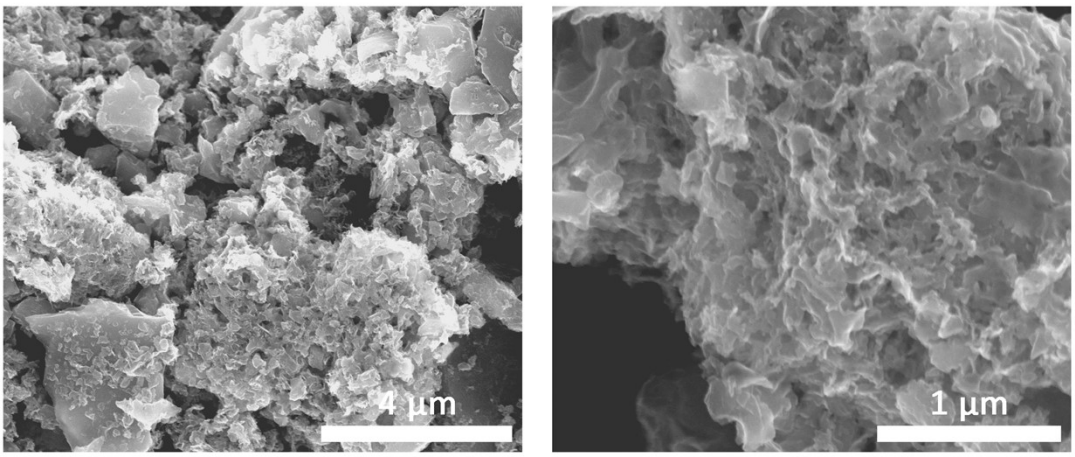

Figure S12. SEM of **Fe@NC(10+800)**.

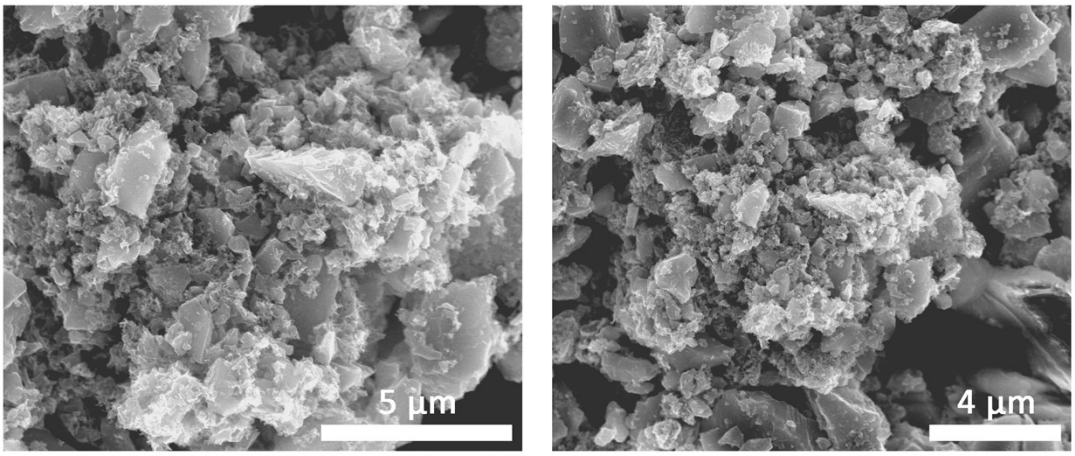

Figure S13. SEM of **Fe@NC(10+900)**.

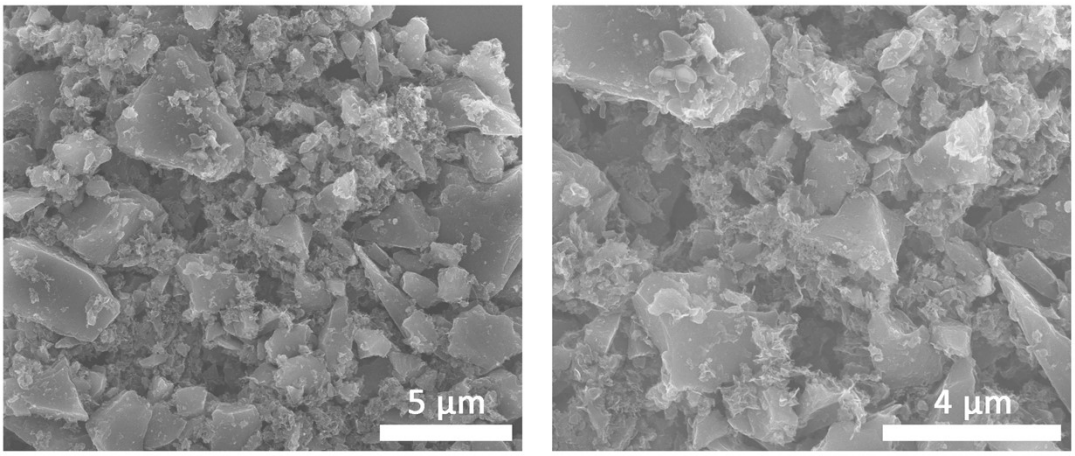

Figure S14. SEM of **Fe@NC(10+1000)**.

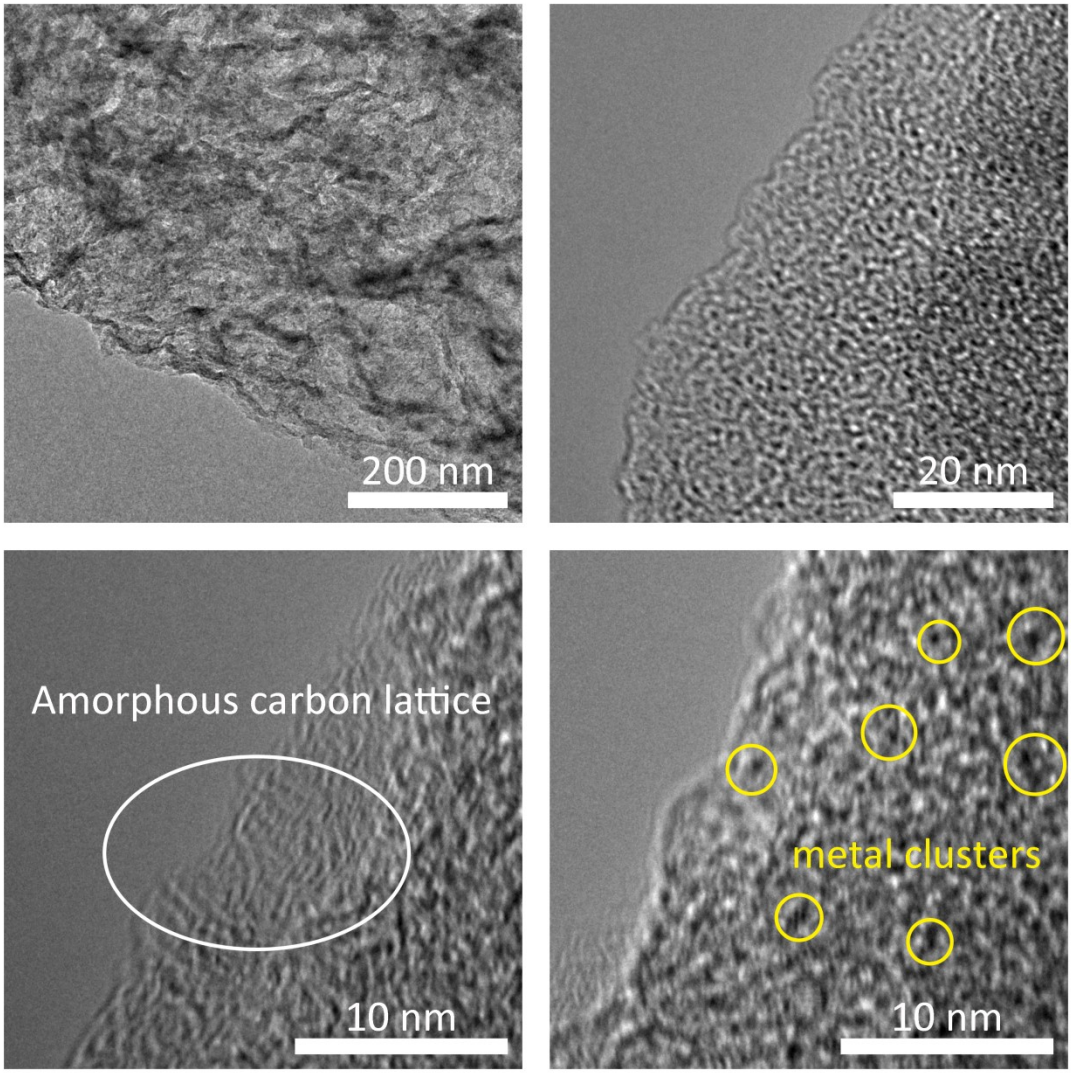

Figure S15. TEM images of **Fe@NC(10+700)**.

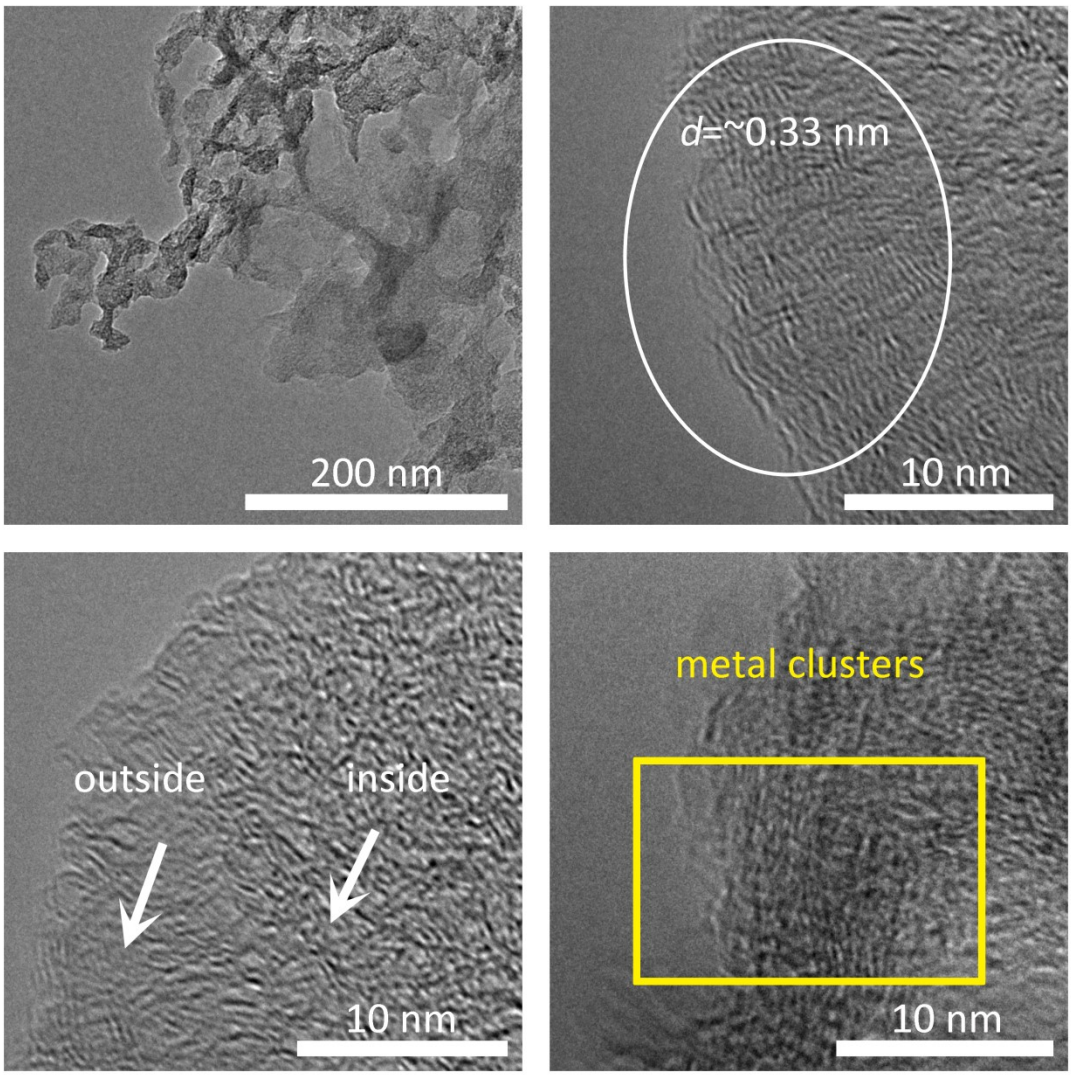

Figure S16. TEM images of **Fe@NC(10+800)**.

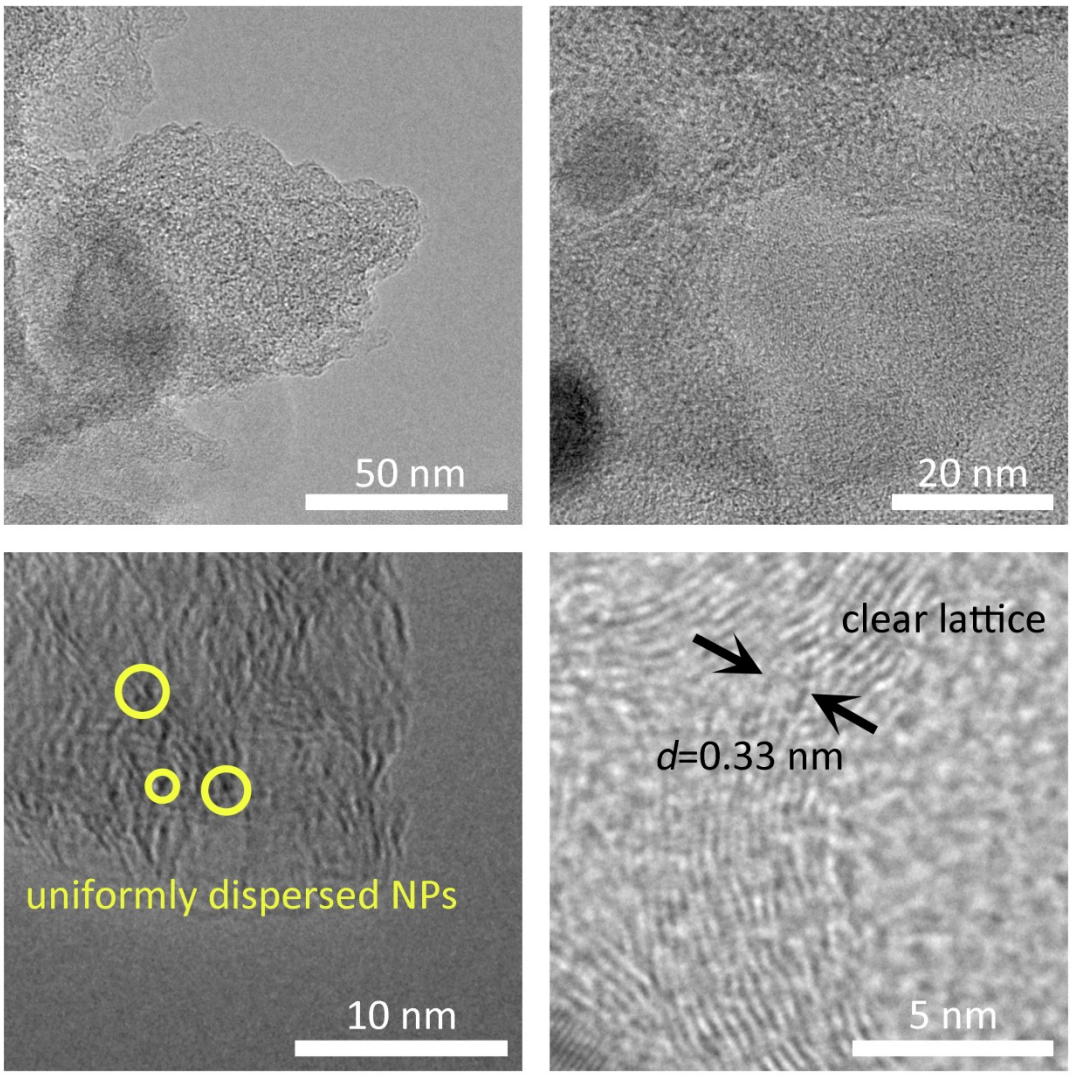

Figure S17. TEM images of **Fe@NC(10+900)**.

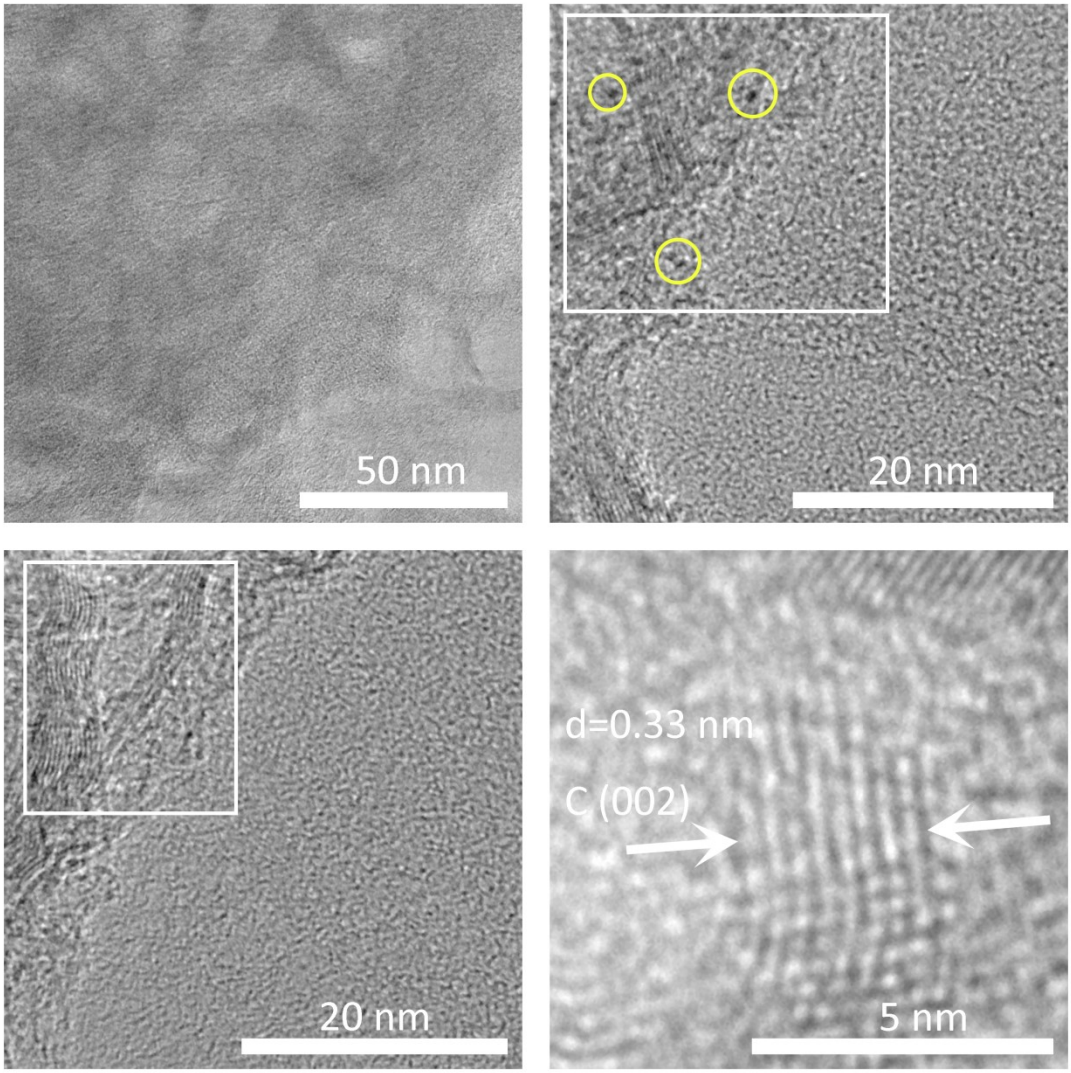

Figure S18. TEM images of **Fe@NC(10+1000)**.

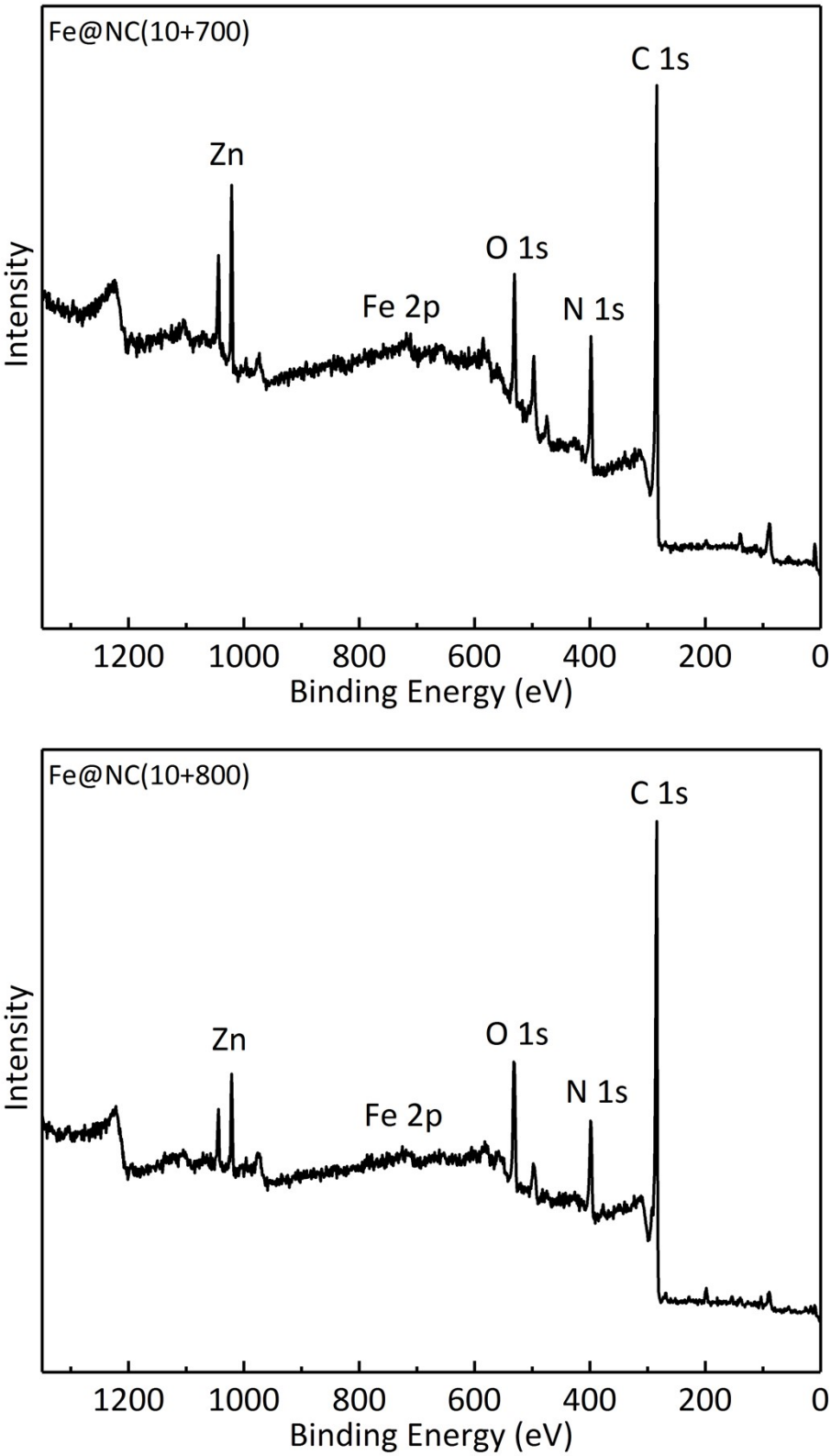

Figure S19. Full XPS survey spectra of **Fe@NC(10+700)** and **Fe@NC(10+800)**.

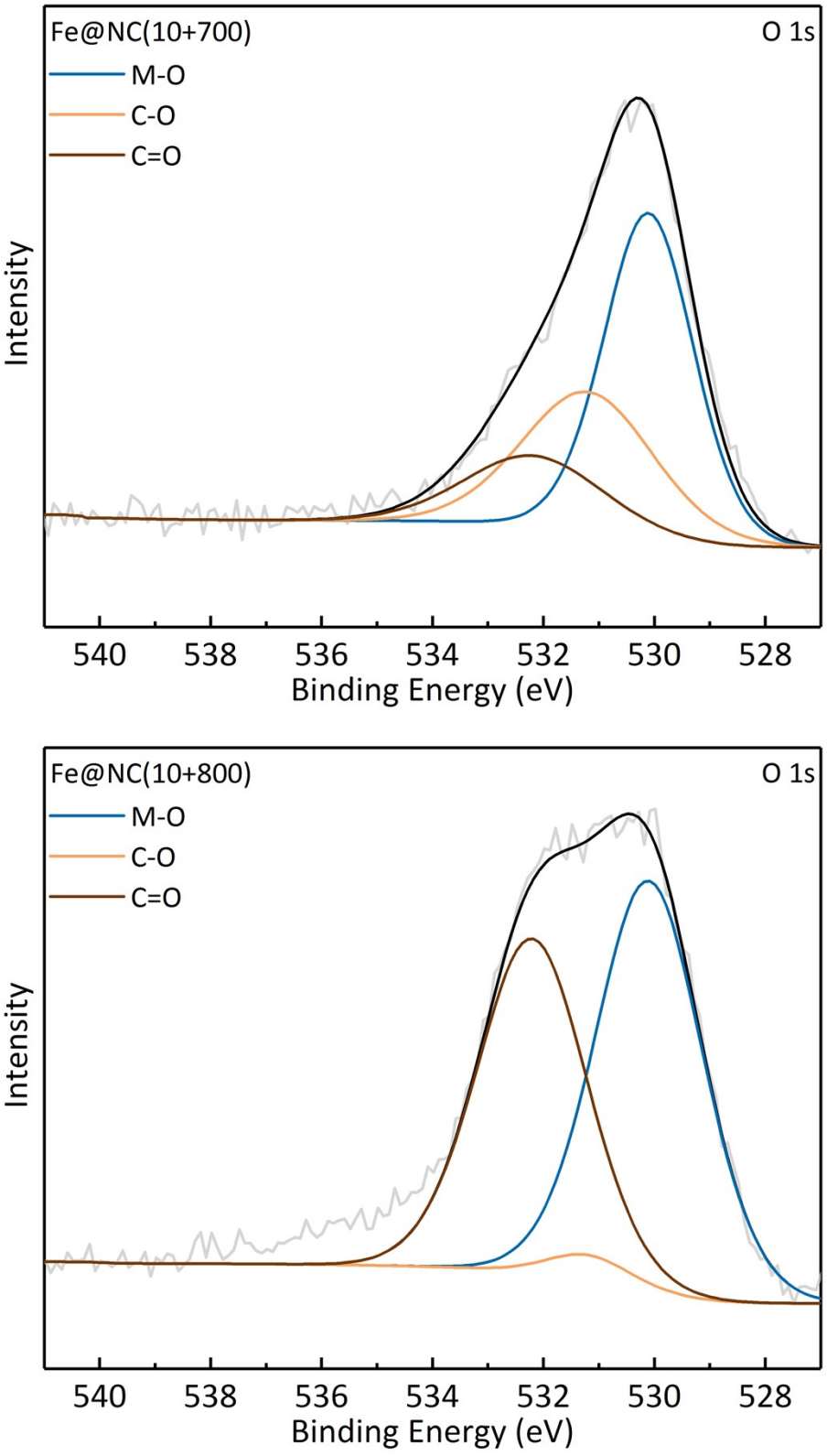

Figure S20. The deconvoluted O 1s survey spectra of **Fe@NC(10+700)** and **Fe@NC(10+800)**.

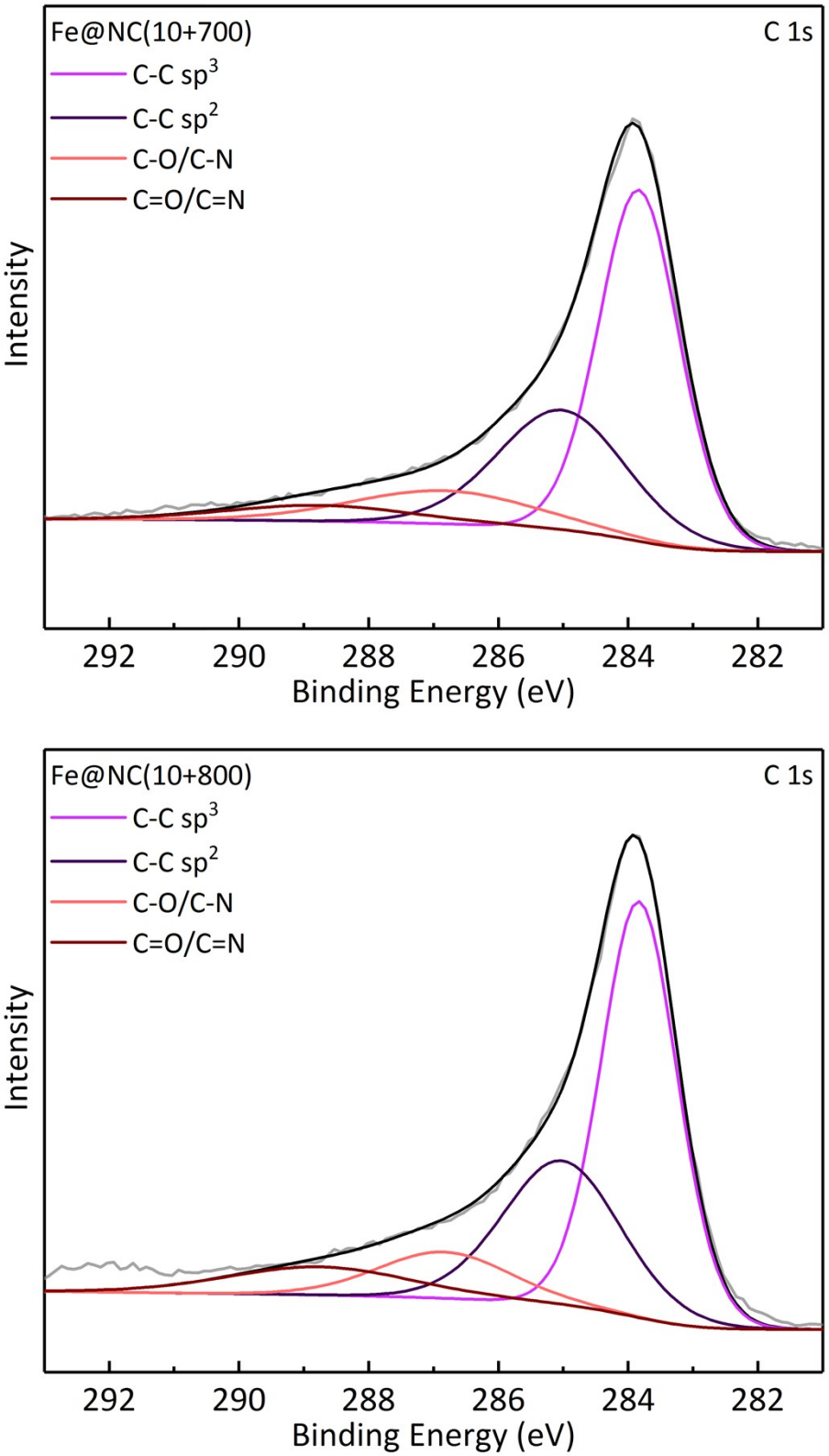

Figure S21. The deconvoluted C 1s survey spectra of **Fe@NC(10+700)** and **Fe@NC(10+800**

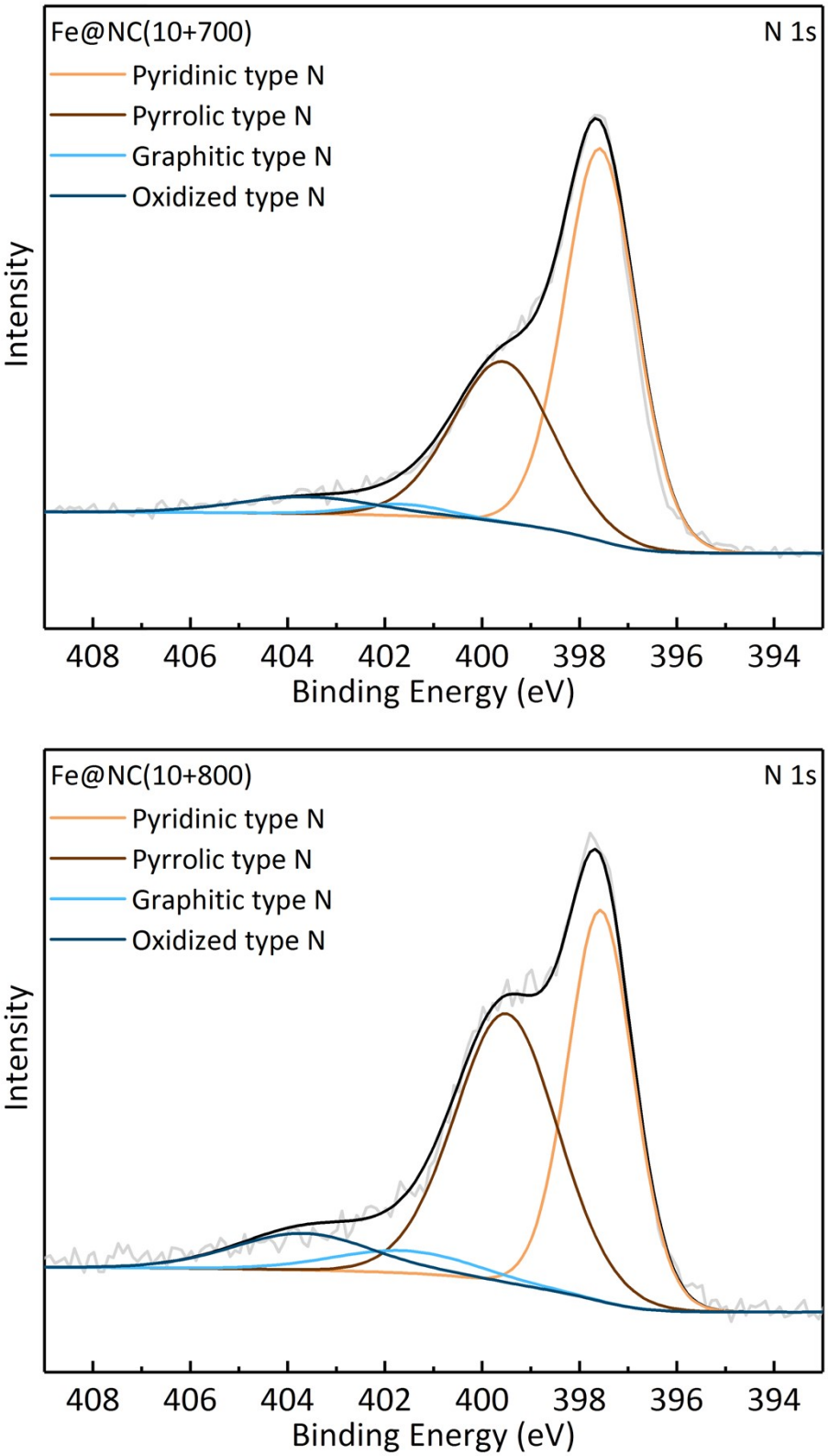

Figure S22. The deconvoluted N 1s survey spectra of **Fe@NC(10+700)** and **Fe@NC(10+800)**.

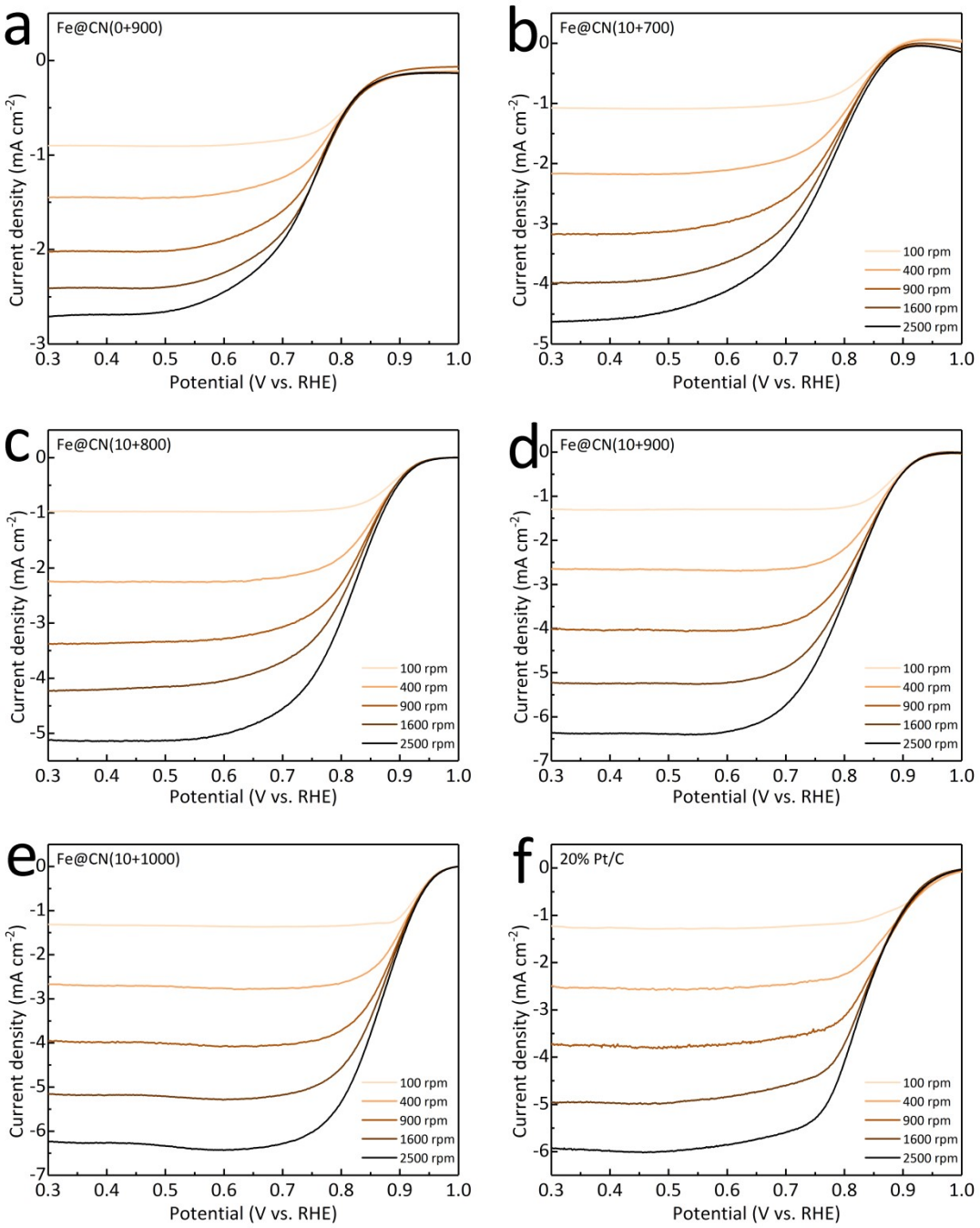

Figure S23. RRDE plots with various rotation speeds at a scan rate of 5 mV s^{-1} in O_2-saturated 0.1 M KOH solution of (a) **Fe@NC(0+900)**, (b) **Fe@NC(10+700)**, (c) **Fe@NC(10+800)**, (d) **Fe@NC(10+900)**, (e) **Fe@NC(10+1000)** and (f) 20% Pt/C.

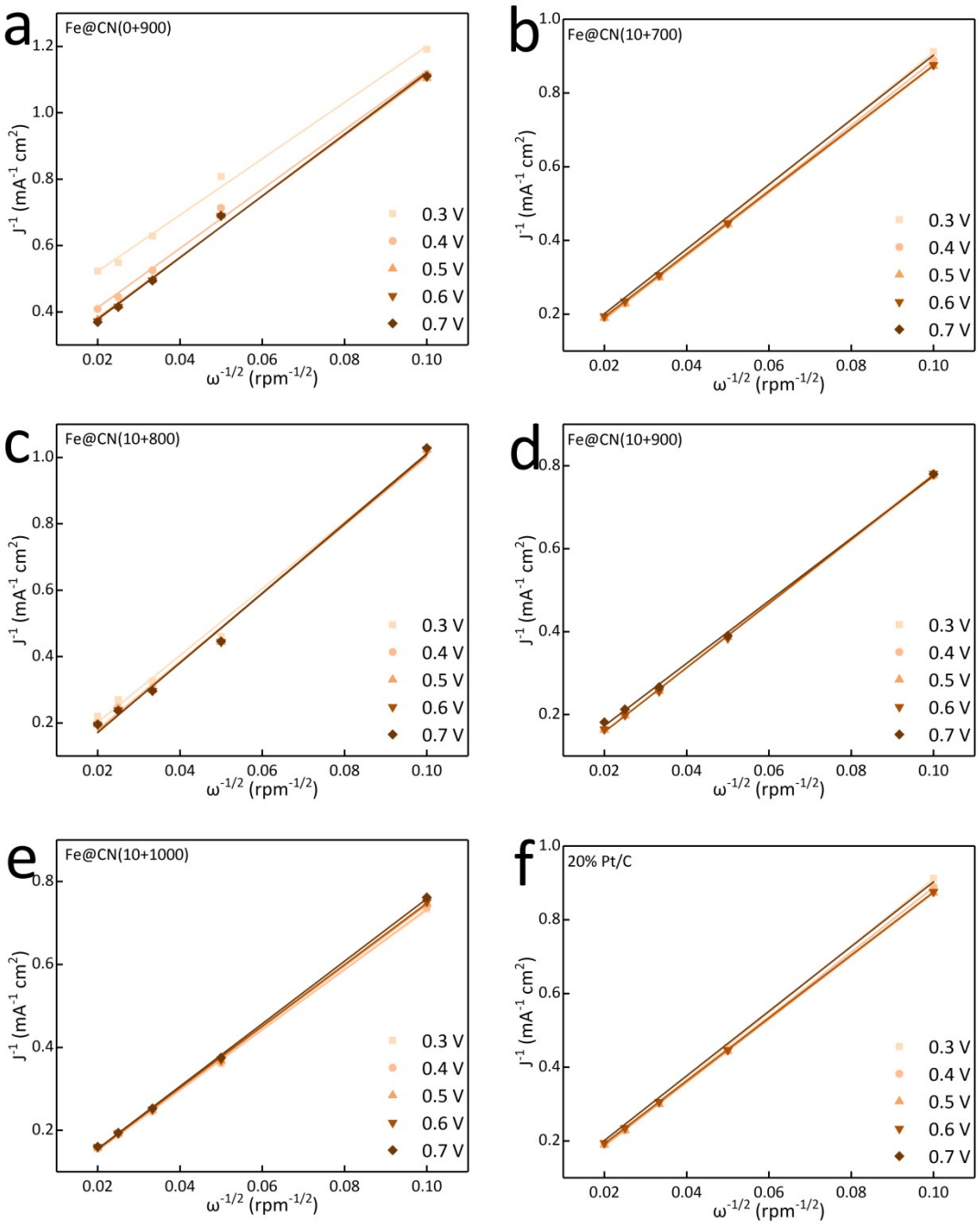

Figure S24. K-L plots at various voltages at 1600 rpm in O_2-saturated 0.1 M KOH solution of (a) **Fe@NC(0+900)**, (b) **Fe@NC(10+700)**, (c) **Fe@NC(10+800)**, (d) **Fe@NC(10+900)**, (e) **Fe@NC(10+1000)** and (f) 20% Pt/C.

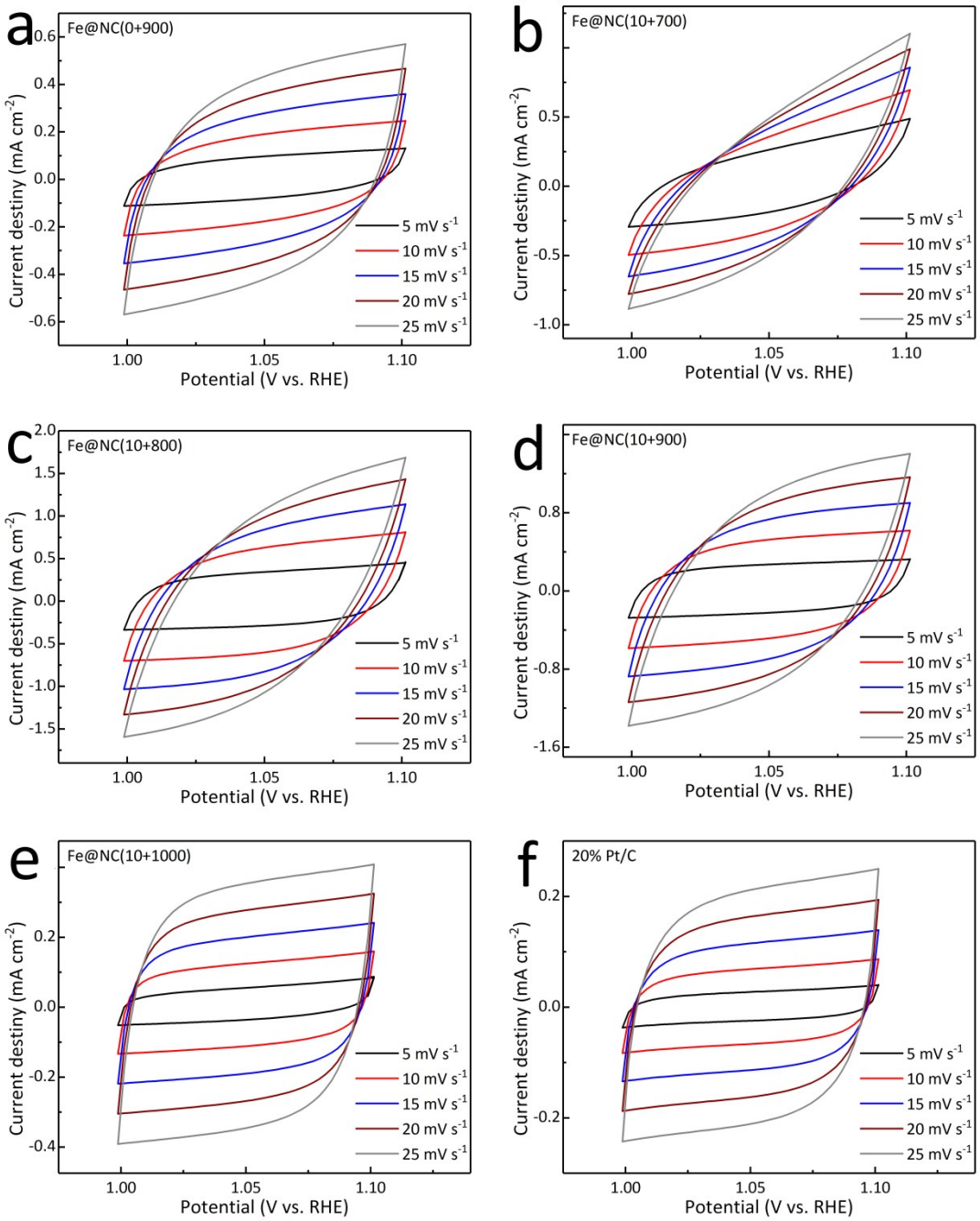

Figure S25. The C_{dl} is calculated from the cyclic voltammograms of (a) **Fe@NC(0+900)**, (b) **Fe@NC(10+700)**, (c) **Fe@NC(10+800)**, (d) **Fe@NC(10+900)**, (e) **Fe@NC(10+1000)** and (f) 20% Pt/C

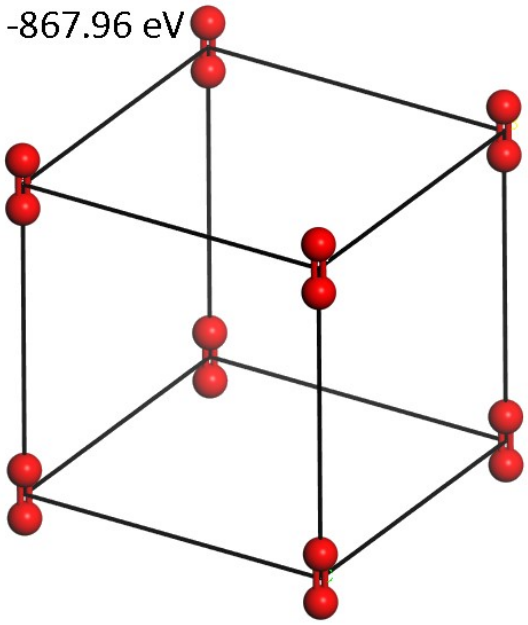

Figure S26. Geometrically optimized model for a O_2.

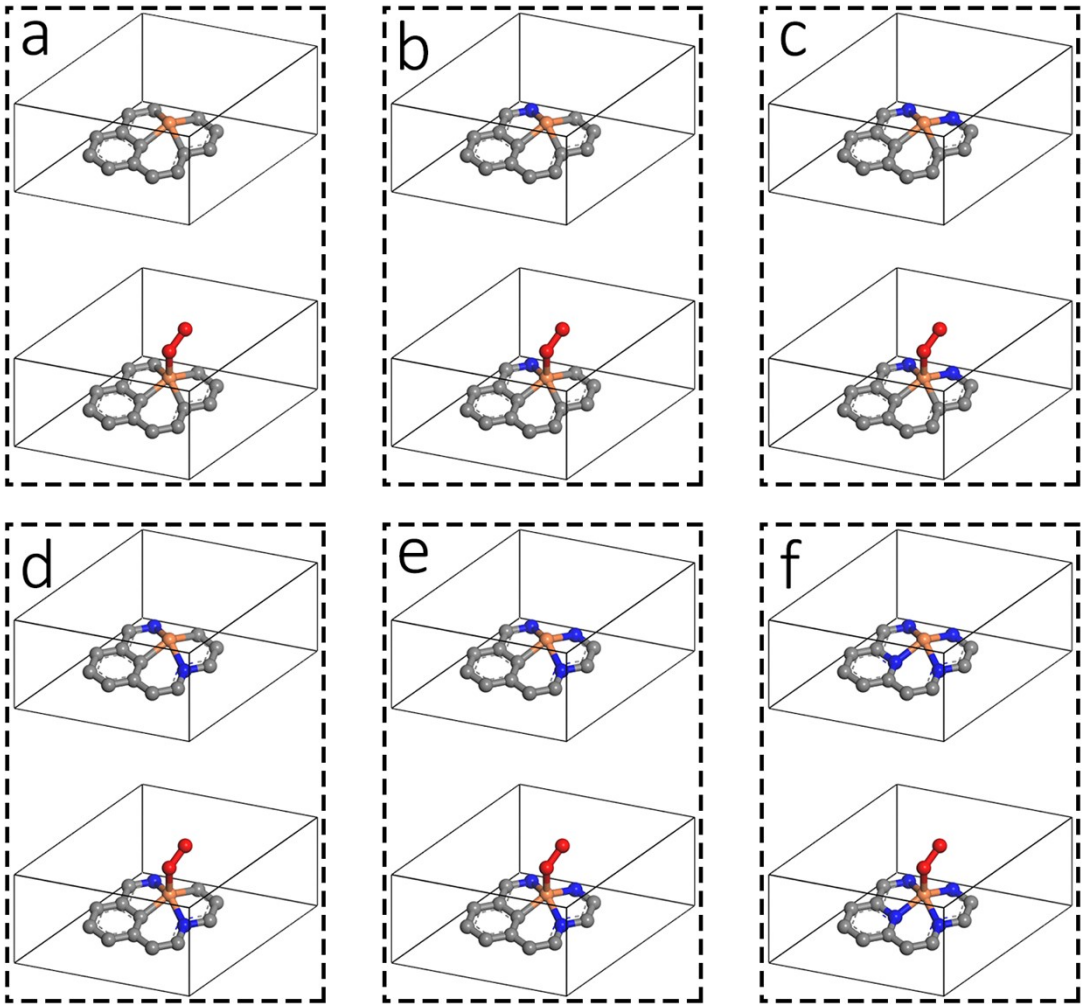

Figure S27. Optimized nanostructures of different 4-coordinate Fe active sites.

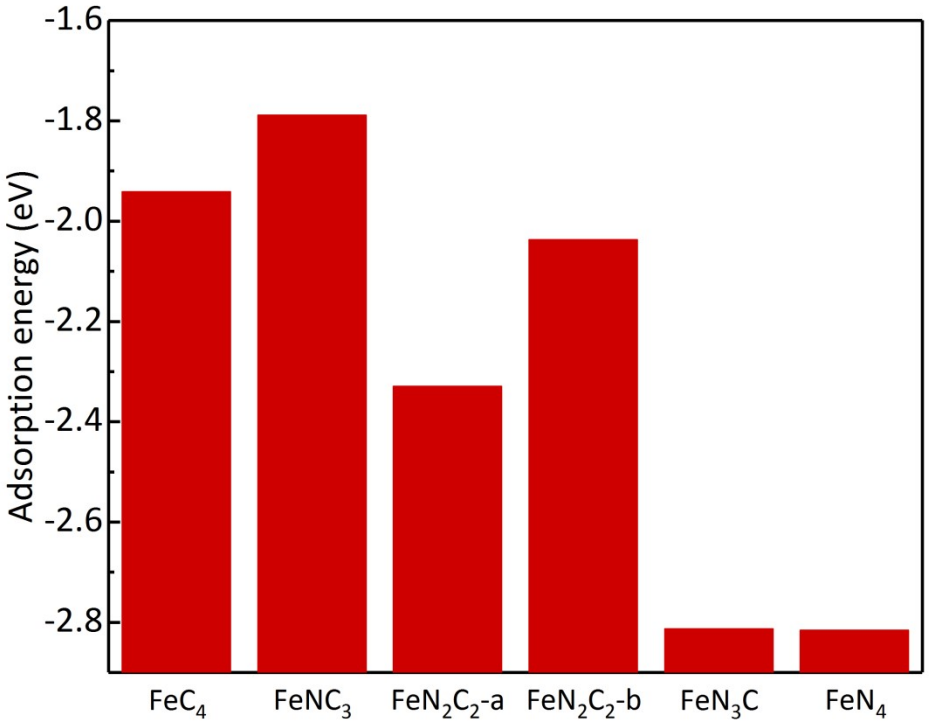

Figure S28. O_2 loaded adsorption energy of FeN_xC_y.

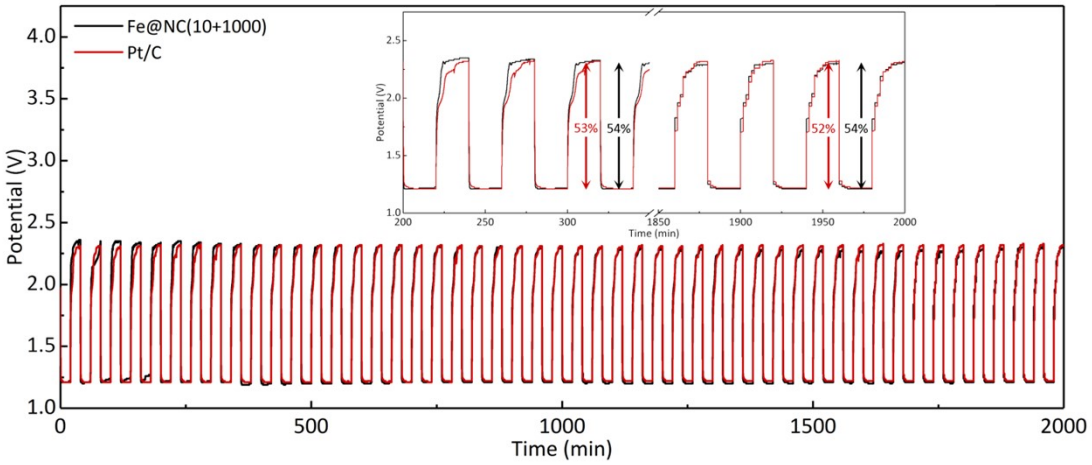

Figure S29. The long-term stability at 5 mA cm^{-2} of the zinc-air battery based on **Fe@NC(10+1000)** and Pt/C.

Table S1. Summary of Crystal Data and Refinement Results for BMM-14.

Items	BMM-14
CCDC	2130792
Formula	$C_{95}H_{70}N_{51}O_{21}Zn_{12}$
Mass	1523.23
crystal system	hexagonal
space group	*P63cm*
a (Å)	46.2077
b (Å)	46.2077
c (Å)	18.6293
α (°)	90.00
β (°)	90.00
γ (°)	120.00
V(Å^3)	34447.3
T (K)	250
Z	12
F(000)	9150.0
R_{int}	0.1619
R_1 (I>2σ(I))	0.1619
wR_2 (all reflections)	0.3658

Table S2. Summary of Gas Sorption Results for BMM-14.

	BET surface area (m^2 g^{-1})	NLDFT micropore volume (ml g^{-1})	NLDFT totalpore volume (ml g^{-1})
Expe_BMM-14	1117.4987	0.5620	0.6991
FePc@BMM-14(0.1)	763.9485	0.3794	0.4647
FePc@BMM-14(1)	679.5249	0.3347	0.4536
FePc@BMM-14(10)	563.0729	0.2817	0.3881

Table S3. O 1s Survey Spectra of Fe@NC(x+y).

	M-O	C-O	C=O
Fe@NC(0+900)	530.1	531.2	532.2
Fe@NC(10+700)	530.1	531.2	532.2
Fe@NC(10+800)	530.1	531.4	532.2
Fe@NC(10+900)	530.1	531.3	532.2
Fe@NC(10+1000)	530.1	531.2	532.2

Table S4. C 1s Survey Spectra of Fe@NC(x+y).

	C-C sp^3	C=C sp^2	C-N	C=N
Fe@NC(0+900)	283.8	285.0	286.9	288.8
Fe@NC(10+700)	283.8	285.0	286.9	288.8
Fe@NC(10+800)	283.8	285.0	286.9	288.8
Fe@NC(10+900)	283.8	285.0	286.9	288.8
Fe@NC(10+1000)	283.8	285.0	286.9	288.8

Table S5. N 1s Survey Spectra of Fe@NC(x+y).

	Pyridinic-N	Pyrrolic-N	Graphitic-N	Oxidized-N
Fe@NC(0+900)	397.6	399.7	401.7	403.6
Fe@NC(10+700)	397.6	399.6	401.8	403.7
Fe@NC(10+800)	397.6	399.6	401.8	403.8
Fe@NC(10+900)	397.6	399.6	401.7	403.8
Fe@NC(10+1000)	397.6	399.7	401.7	403.6

Table S6. Zn 2p Survey Spectra of Fe@NC(x+y).

	Zn(II) $2p_{3/2}$	**Zn(II) $2p_{1/2}$**
Fe@NC(0+900)	1020.78	1043.83
Fe@NC(10+700)	1020.68	1043.68
Fe@NC(10+800)	1020.48	1043.58
Fe@NC(10+900)	1020.93	1044.23
Fe@NC(10+1000)	1020.98	1044.18

Table S7. Fe 2p Survey Spectra of Fe@NC(x+y).

	Fe(0) $2p_{3/2}$	Fe(II) $2p_{3/2}$	Fe(III) $2p_{3/2}$	Fe(0) $2p_{1/2}$	Fe(II) $2p_{1/2}$	Fe(III) $2p_{1/2}$
Fe@NC(10+700)	706.88	709.48	712.28	720.58	722.18	724.58
Fe@NC(10+800)	706.98	709.58	712.38	720.68	722.28	724.68
Fe@NC(10+900)	706.78	709.28	711.83	720.08	721.83	724.03
Fe@NC(10+1000)	705.98	708.58	711.08	719.38	721.18	723.28

Table S8. Comparison of ORR Performance for Fe@NC(10+900/1000) with Reported Carbon-Based Electrocatalysts.

Catalyst	E_{onset} (V vs. RHE)	$E_{1/2}$ (V vs. RHE)	J_{1600} (mA cm^{-1})	Reference
C-CZ-4-1000	1.03	0.89	-5.9	1
Co-C@NWCs	0.94	0.83	-4.51	2
CoHNCS-0.2	0.94	0.82	-5.8	3
Co,N-CNF	0.88	0.81	-5.7	4
Fe-N-DSC	1.03	0.83	/	5
Fe-N-RFC_C240	1.00	0.91	-5.5	6
Fe-N-C HNSs	1.05	0.84	-5.8	7
Fe@NC(10+900)	0.94	0.82	-5.2	This work
Fe@NC(10+1000)	0.97	0.88	-5.2	This work

1. L. Ge, Y. Yang, L. Wang, W. Zhou, R. D. Marco, Z. G. Chen, J. Zou, Z. H. Zhu, High activity electrocatalysts from metal-organic framework-carbon nanotube templates for the oxygen reduction reaction, *Carbon* **2015**, 82, 417-424.

2. Y. Y. Li, F. Y. Cheng, J. N. Zhang, Z. M. Chen, Q. Xu, S. J. Guo, Cobalt-Carbon Core-Shell Nanoparticles Aligned on Wrinkle of N-Doped Carbon Nanosheets with Pt-Like Activity for Oxygen Reduction, *Small* **2016**, 12, 2839-2845.

3. X. D. Chen, K. Shen, J. Y. Chen, B. B. Huang, D. N. Ding, L. Zhang, Y. W. Li, Rational design of hollow N/Co-doped carbon spheres from bimetal-ZIFs for high-efficiency electrocatalysis, *Chemical Engineering Journal* **2017**, 330, 736-745.

4. L. Shang, H. J. Yu, X. Huang, T. Bian, R. Shi, Y. F. Zhao, G. I. N. Waterhouse, L. Z. Wu, C. H. Tung, T. R. Zhang, *Advance Materials* **2016**, 28, 1668-1674.

5. Z. Huang, H. Y. Pan, W. J. Yang, H. H. Zhou, N. Gao, C. P. Fu, S. C. Li, H. X. Li, Y. F. Kuang, *ACS Nano* **2018**, 12, 208-216.

6. M. Kim, H. S. Kim, S. J. Yoo, W. C. Yoo, Y.-E. Sung, The role of pre-defined microporosity in catalytic site formation for the oxygen reduction reaction in iron- and nitrogen-doped carbon materials, *Journal of Materials Chemistry A* **2017**, 5, 4199-4206.

7. Y. F. Chen, Z. J. Li, Y. B. Zhu, D. M. Sun, X. E. Liu, L. Xu, Y. W. Tang, Atomic Fe Dispersed on N-Doped Carbon Hollow Nanospheres for High-Efficiency Electrocatalytic Oxygen Reduction, *Advance Materials* **2019**, 31, 1806312.